

Bloch-type magnetic skyrmions in two-dimensional lattice

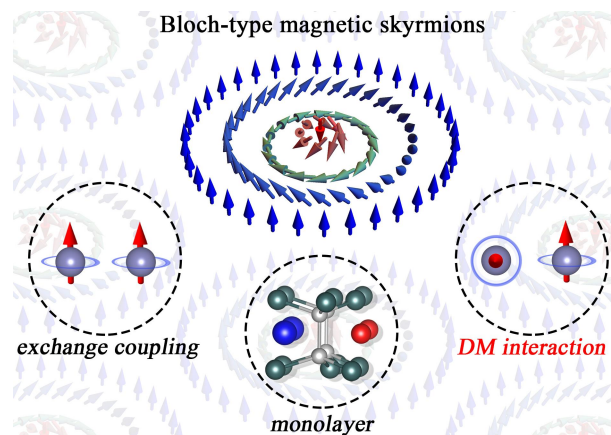
Wenhui Du, Kaiying Dou, Ying Dai*, Baibiao Huang, Yandong Ma*

School of Physics, State Key Laboratory of Crystal Materials, Shandong University, Shandan Street 27, Jinan 250100, China

*Corresponding author: daiy60@sina.com (Y.D.); yandong.ma@sdu.edu.cn (Y.M.)

Abstract

Magnetic skyrmions in two-dimensional lattice are a prominent topic of condensed matter physics and material science. Current research efforts in this field are exclusively constrained to Néel-type and antiskyrmion, while Bloch-type magnetic skyrmions are rarely explored. Here, we report the discovery of Bloch-type magnetic skyrmions in two-dimensional lattice of $\text{MnInP}_2\text{Te}_6$, using first-principles calculations and Monte-Carlo simulations. Arising from the joint effect of broken inversion symmetry and strong spin-orbit coupling, monolayer $\text{MnInP}_2\text{Te}_6$ presents large Dzyaloshinskii-Moriya interaction. This, along with ferromagnetic exchange interaction and out-of-plane magnetic anisotropy, gives rise to skyrmion physics in monolayer $\text{MnInP}_2\text{Te}_6$, without needing magnetic field. Remarkably, different from all previous works on two-dimensional lattice, the resultant magnetic skyrmions feature Bloch-type, which is protected by D_3 symmetry. Furthermore, the Bloch-type magnetic bimerons are also identified in monolayer $\text{MnTlP}_2\text{Te}_6$. The phase diagrams of these Bloch-type topological magnetisms under magnetic field, temperature and strain are mapped out. Our results greatly enrich the research on magnetic skyrmions in two-dimensional lattice.



Keywords: magnetic skyrmions, Bloch-type, ferromagnetic, DMI, first-principles

Introduction

Magnetic skyrmions are nanoscale chiral spin textures with nontrivial real-space topology [1-5]. The topological nature is accompanied with an integer topological charge Q and decoupled from the crystal lattice. Since the initial experimental observation in 2009 [6], this swirling configuration has attracted great attention and spurred rapid development due to a variety of exotic characteristics, such as topologically robust against defects, solitonic feature and efficient current-driven dynamics [7,8]. These appealing properties provide not only new opportunities for exploring fundamental topological physics but also great potential for future spintronics devices [9-11]. In recent years, with the rise of two-dimensional (2D) materials [12-16] and discovery of magnetism in monolayers CrI_3 [17], VSe_2 [18,19] and Fe_3GeTe_2 [20], many efforts are devoted to investigating skyrmion physics in 2D lattices, and magnetic skyrmions in 2D lattices have been the topic of intense research in condensed matter physics and material science [21-35].

According to the inner spin arrangements of vorticity ω and helicity γ , magnetic skyrmions can debut in three typical cases of $(\omega, \gamma) = (1, 0 \text{ or } \pi), (1, \pm\pi/2)$ and $(-1, 0 \text{ or } \pm\pi/2 \text{ or } \pi)$, corresponding to Néel-type, Bloch-type and antiskyrmion, respectively [36]. These distinct magnetic skyrmions are equivalently attractive and exhibit fertile physics. The variation of magnetic skyrmions generally arises from Dzyaloshinskii-Moriya interaction (DMI) [37,38]. Such short-range antisymmetric exchange interaction, in fact, acts as a chiral interaction and fixes the specific rotational sense of spins. Driven by various bulk and interface DMI, all the three types of magnetic skyrmions are extensively explored in conventional B20 bulk and thin-film systems [39-48]. Nevertheless, magnetic skyrmions reported in 2D lattice, in most cases, are constrained to Néel-type [21-31], and only a few 2D systems with antiskyrmion are also reported [32,33]. Actually, up to now, Bloch-type magnetic skyrmions in 2D lattice which requires special DMI have not been reported yet. From the perspective of fundamental research, it is essential to explore such Bloch-type magnetic skyrmions in two-dimensional lattice.

In this work, through first-principles calculations and Monte-Carlo (MC) simulations, we report the identification of Bloch-type magnetic skyrmions in 2D lattice of $\text{MnInP}_2\text{Te}_6$. Due to the combined effect of broken inversion symmetry and strong spin-orbit coupling (SOC), large DMI is obtained in monolayer $\text{MnInP}_2\text{Te}_6$. The competition between DMI and ferromagnetic exchange interaction as well as out-of-plane magnetic anisotropy results in skyrmion physics in $\text{MnInP}_2\text{Te}_6$ in the absence of magnetic field. Importantly, protected by D_3 symmetry, the resultant magnetic

skyrmions feature the intriguing Bloch-type. Meanwhile, Bloch-type magnetic bimerons are also observed in monolayer $\text{MnTlP}_2\text{Te}_6$. In addition, the evaluations of these Bloch-type topological magnetisms under magnetic field, temperature and strain are systematically discussed.

Results and Discussion

Figure 1(a) presents the crystal structure of monolayer MnXP_2Te_6 ($X=\text{In, Tl}$), which is isostructural to MnPTe_3 [49]. Its unit cell contains one Mn, one X, two P and six Te atoms. Each Mn/X atom is octahedrally coordinated with six Te atoms, forming a hexagonal lattice with the space group $P312$ (D_3); see **Figure 1(b)**. Obviously, the inversion symmetry of monolayer MnXP_2Te_6 is broken. The lattice constants of monolayer MnXP_2Te_6 are summarized in **Table S1**. The dynamic and thermal stabilities of monolayer MnXP_2Te_6 are confirmed by performing the phonon spectra calculations (**Figure S1**) and AIMD simulations (**Figure S2**), respectively.

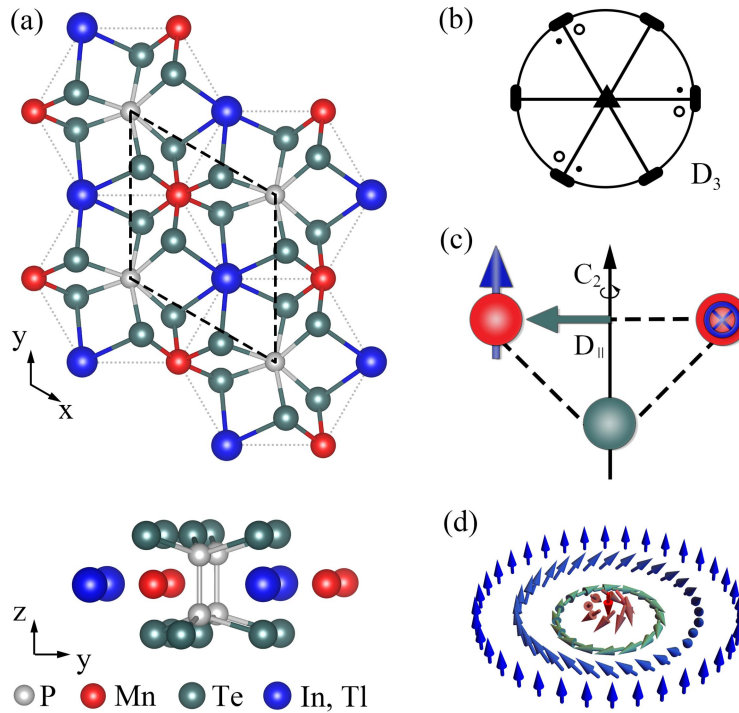


Figure 1. (a) Crystal structure of monolayer MnXP_2Te_6 from top and side views. (b) Equatorial plane projection of the point group for monolayer MnXP_2Te_6 . (c) Schematic illustration of DMI acting on the adjacent magnetic moments of monolayer MnXP_2Te_6 . (d) Schematic representation of Bloch-type spin configuration.

The valence electron configurations of Mn and In/Tl atoms are $3d^54s^2$ and $5s^25p^1/6s^26p^1$, respectively. Upon coordinating with the neighboring Te atoms, each Mn atom donates three

electrons, while each X atom denotes one electron, which would generate the formal oxidation states of +3 and +1 for Mn and X atoms, respectively. Note that under distorted octahedral coordination environment, Mn-3d orbitals roughly split into two groups, i.e., two high-lying e_g ($d_{xy}, d_{x^2-y^2}$) and three low-lying t_{2g} (d_{xz}, d_{yz}, d_{z^2}) orbitals. As d electrons of Mn favor high-spin configuration, according to the Hund's rule and Pauli exclusion principle, the four left electrons would half-fill three t_{2g} and one e_g orbitals. This would yield a magnetic moment of $4 \mu_B$ on each Mn atom. Our first-principles calculations indeed show that the magnetic moment per unit cell is $4 \mu_B$ and mainly localized on Mn atoms (see **Figure S3**).

To characterize the detailed interaction between the magnetic moments of monolayer MnXP_2Te_6 , we introduce the following Heisenberg spin Hamiltonian:

$$H = \sum_{\langle i,j \rangle} \mathbf{D}_{ij} \cdot (\mathbf{S}_i \times \mathbf{S}_j) - J \sum_{\langle i,j \rangle} \mathbf{S}_i \cdot \mathbf{S}_j - \lambda \sum_{\langle i,j \rangle} S_i^z S_j^z - K \sum_i (S_i^z)^2 - m B_a \sum_i S_i^a \quad (1)$$

Here, \mathbf{S}_i is unit vector representing local spin of Mn atom at site i . $\langle i, j \rangle$ represents nearest-neighbor sites. \mathbf{D}_{ij} , J , λ and K stand for parameters of DMI, Heisenberg isotropic exchange, anisotropic symmetric exchange and single ion anisotropy, respectively. The last term is the Zeeman energy, where m and B_a indicate on-site magnetic moment of Mn atom and external magnetic field along the a ($a = x, z$) direction, respectively. In view of the D_3 symmetry, as shown in **Figure 1(c)**, there is a two-fold rotation axis vertically passing through the middle of the bond between two neighboring Mn atoms. According to the Moriya's rule [38], the DMI vector \mathbf{D}_{ij} for the nearest-neighbor Mn atoms is perpendicular to this two-fold rotation axis, which can be expressed as $\mathbf{D}_{ij} = d_{\parallel} \mathbf{u}_{ij} + d_{\perp} \mathbf{z}$ with \mathbf{u}_{ij} representing the unit vector pointing from site i to j and \mathbf{z} being the out-of-plane unit vector. Due to the D_3 symmetry, the out-of-plane component d_{\perp} presents a staggered arrangement for the six nearest-neighbor Mn atoms, which renders it negligible in average. It is worth emphasizing that the in-plane component d_{\parallel} is parallel to the bond between two adjacent Mn atoms. It makes the spins rotating in a plane perpendicular to the radial direction; see **Figure 1(d)**. This is different from most of the previous works wherein the DMI forces the spins rotating in a plane along a radial direction [21-31]. As we will show below, such particularly DMI favors Bloch-type magnetic skyrmions. To obtain the in-plane component d_{\parallel} , the left- and right-hand spin-spiral configurations are considered, as shown in **Figure 2(a)**. Strikingly, d_{\parallel} in monolayer $\text{MnInP}_2\text{Te}_6$ ($\text{MnTIP}_2\text{Te}_6$) is calculated to be 2.87 (5.79) meV, which comparable with or even remarkably larger

than that reported in previous studies [21-34].

To get more insights into the large DMI in monolayer MnXP_2Te_6 , we investigate the atomic resolved SOC energy difference ΔE_{soc} between two different spin-spiral configurations. As shown in **Figure 2(c)**, the DMI is mainly contributed by Te atom, while other atoms make only slight contributions. This suggests that the Fert-Levy mechanism [50,51] plays a dominant role for inducing DMI in monolayer MnXP_2Te_6 . By considering the strong SOC strength within Te atom, we can understand why large DMI is obtained in both systems. Another point we can see from **Figure 2(c)** is that the magnitude of ΔE_{soc} for Te atom in monolayer $\text{MnTlP}_2\text{Te}_6$ is pronouncedly larger than that in monolayer $\text{MnInP}_2\text{Te}_6$. This might be related to the relatively large atomic radius of Tl atom, which exacerbates the bipartite asymmetry in monolayer $\text{MnTlP}_2\text{Te}_6$ and thus leads to the large magnitude of ΔE_{soc} and DMI.

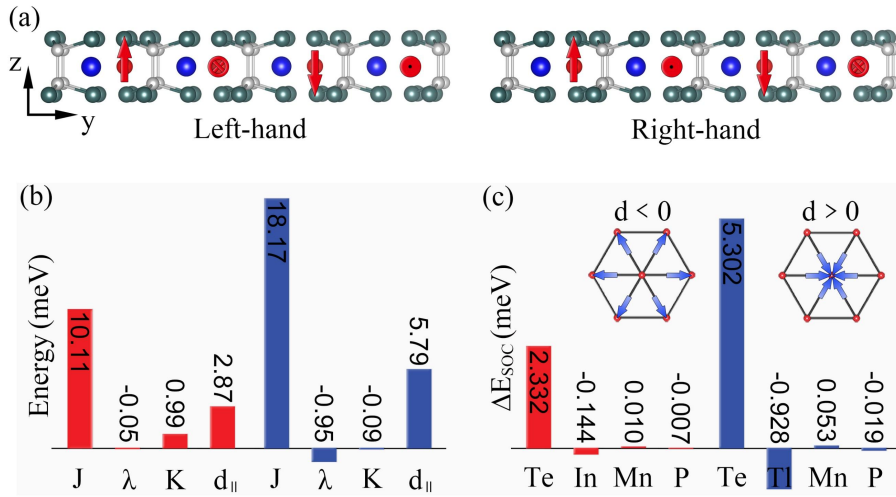


Figure 2. (a) Left and right-hand spin-spiral configurations used to obtain the in-plane DMI parameter d_{\parallel} and atomic projected SOC energy. (b) The calculated J , λ , K and d_{\parallel} of monolayer MnXP_2Te_6 . (c) SOC energy projected on atoms (ΔE_{soc}) for monolayer MnXP_2Te_6 . Insets in (c) show the in-plane DMI vectors $d_{\parallel} \mathbf{u}_{ij}$ (blue vectors) between the nearest-neighbor Mn atoms (red balls).

To obtain J , λ and K , we considered four different magnetic configurations as displayed in **Figure S4**. The isotropic exchange parameter J is calculated to be 10.11 and 18.17 meV, respectively, for monolayer $\text{MnInP}_2\text{Te}_6$ and $\text{MnTlP}_2\text{Te}_6$. This indicates FM exchange interaction is favorable for neighboring magnetic atoms for both systems. The single ion anisotropy K consists of two parts: one is magnetocrystalline anisotropy K_{MCA} and another is magnetic shape anisotropy K_{MSA} , i.e., $K = K_{MCA} + K_{MSA}$. The former arises from SOC, while the latter results from

magnetostatic dipole-dipole interaction and usually prefers in-plane magnetization. For monolayer $\text{MnInP}_2\text{Te}_6$, K and λ are calculated to be 0.99 and -0.05 meV, respectively, which prefer out-of-plane and in-plane magnetizations. Note that magnetic anisotropy is determined by the combined effect of K and λ . Obviously, the positive K is much larger than λ , which indicates that the spins in monolayer $\text{MnInP}_2\text{Te}_6$ tend to align along the out-of-plane orientation. Different from monolayer $\text{MnInP}_2\text{Te}_6$, monolayer $\text{MnTlP}_2\text{Te}_6$ has $K = -0.09$ meV and $\lambda = -0.95$ meV, suggesting the preference of in-plane magnetization. Based on the obtained J , λ , and K , we study the Curie temperature T_C of monolayer $\text{MnInP}_2\text{Te}_6$ and $\text{MnTlP}_2\text{Te}_6$, which are estimated to be 130 and 230 K, respectively (Figure S5). Figure S6 shows the band structures of monolayer MnXP_2Te_6 . It can be seen that the spin-up bands cross the Fermi level, while the spin-down bands lie away from the Fermi level. This leads to a fully spin polarization for the conduction electrons around the Fermi level. Therefore, monolayer MnXP_2Te_6 exhibits 2D ferromagnetic half-metallic nature.

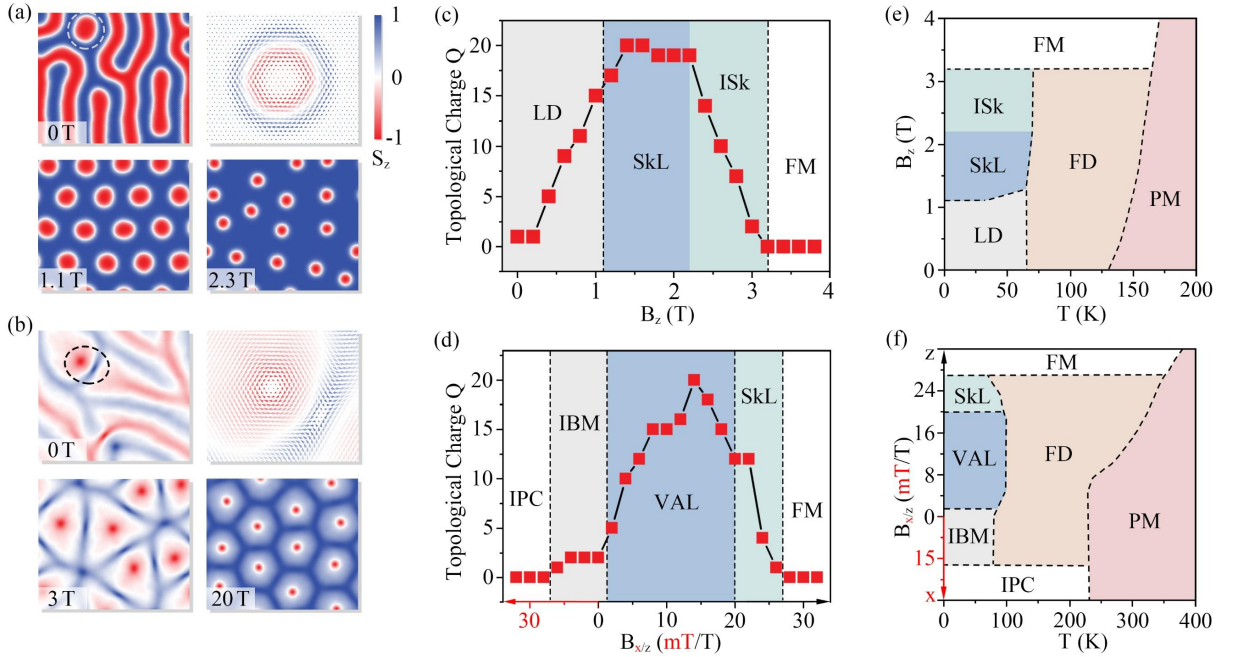


Figure 3. Spin textures of monolayer (a) $\text{MnInP}_2\text{Te}_6$ and (b) $\text{MnTlP}_2\text{Te}_6$ without and with applying magnetic field at 0 K. Top-right panels in (a, b) shows the enlarged spin distribution in (a) skyrmion and (b) bimeron. Colors indicate the out-of-plane spin components and arrows denote the in-plane components. Evolutions of topological charge Q of monolayer (c) $\text{MnInP}_2\text{Te}_6$ and (d) $\text{MnTlP}_2\text{Te}_6$ as a function of magnetic field. Phase diagrams of monolayer (e) $\text{MnInP}_2\text{Te}_6$ and (f) $\text{MnTlP}_2\text{Te}_6$ under temperature and magnetic field.

Next, we perform parallel tempering MC simulations to explore the topological spin textures in

monolayer MnXP_2Te_6 based on the first-principles parametrized Hamiltonian of Eq. (1). Topological charge Q is employed to characterize the non-trivial nature of the spin structures, which can be described as $Q = \frac{1}{4\pi} \int \mathbf{m} \cdot \left(\frac{\partial \mathbf{m}}{\partial x} \times \frac{\partial \mathbf{m}}{\partial y} \right) dx dy$ [52]. Here, \mathbf{m} is the normalized magnetization vector. As shown in **Figure 3(a)**, the spin texture with an isolated magnetic skyrmion and labyrinth domains is observed in monolayer $\text{MnInP}_2\text{Te}_6$ in the absence of external magnetic field. Such a mixed phase is referred to as labyrinth domain (LD) phase below. Remarkably, from the enlarged magnetic skyrmion shown in the top-right panel of **Figure 3(a)**, we can see that the spins rotate in a plane perpendicular to the radial direction. This confirms that the long-sought Bloch-type magnetic skyrmions are achieved in monolayer $\text{MnInP}_2\text{Te}_6$. The underlying physics is related to the particularly DMI interaction discussed above. While for monolayer $\text{MnTlP}_2\text{Te}_6$, as shown in **Figure 3(b)**, the spin texture with isolated Bloch-type magnetic bimerons (IBM phase) appears in the absence of magnetic field. The difference between them can be attributed to the different magnetic anisotropies.

We then investigate the influence of magnetic field on the topological spin textures of monolayer MnXP_2Te_6 . For monolayer $\text{MnInP}_2\text{Te}_6$, with increasing out-of-plane magnetic field (B_z), the labyrinth domains gradually shrink and split into more skyrmions; see **Figure 3(a)**. When B_z reaches at 1.1 T, the labyrinth domains completely disappear, forming skyrmion lattice (SkL) phase. Such intriguing SkL phase can be maintained within the magnetic field range of 1.1-2.2 T. When further increasing B_z to 2.2-3.2 T, the ordered array of skyrmions is destroyed, forming isolated skyrmion (ISk) phase. Concerning the density of skyrmions, as shown in **Figure 3(c)**, it increases as the B_z increases from 0 T to 1.4 T and remains mostly steady under 1.4-2.2 T. Upon increasing B_z larger than 2.2 T, the density of magnetic skyrmions decreases significantly, and drops to zero at 3.2 T, which corresponds to the trivial FM phase. The physics underlying this evolution arises from compensation effect of B_z that enhances spin collinear arrangement.

Unlike monolayer $\text{MnInP}_2\text{Te}_6$, due to the large in-plane magnetization, the topological spin textures of monolayer $\text{MnTlP}_2\text{Te}_6$ are not so sensitive to B_z . As shown in **Figure 3(d)**, the IBM phase can be preserved within the range of 0-1.5 T. By further increasing B_z larger than 1.5 T, the vortex-antivortex loops (VAL) appear; see **Figure 3(b)**. With increasing B_z to 0-14 T, the topological charge Q rises gradually, corresponding to an increase in the density of vortices. This phenomenon is attributed to the fact that B_z weakens the energetic advantage of in-plane

magnetization contributed by magnetic anisotropy. In VAL region, with increasing B_z from 1.5 to 20 T, the blue vortices and antivortices gradually expand into FM background, and eventually the red vortices evolve into Bloch-type skyrmions at 20 T, forming the SkL phase. As shown in **Figure 3(d)**, under B_z of 14-27 T, the topological charge Q decreases gradually, and reduce to zero at 27 T, corresponding to the transformation into trivial FM phase. In contrast the cases of B_z , topological spin textures in monolayer MnTIP₂Te₆ are more sensitive to the in-plane magnetic field (B_x). We can see from **Figure 3(d)** that the IBM phase can be stable only within the B_x range of 0-18 mT. Upon increasing B_x larger than 18 mT, the bimerons are completely magnetized into trivial spin pattern superimposed by in-plane cycloidal structure (IPC phase) and small out-of-plane waved spin pattern [25], see **Figure S7**.

To get further insight into the thermal stability of these topological spin structures, we establish the T-B magnetic phase diagrams, which are displayed in **Figures 3(e,f)**. In addition to various magnetic phases mentioned above, two extra phases emerge under temperature, i.e., fluctuation-disorder (FD) phase (wherein the topological stability of spin configuration is damaged by thermal fluctuations) and paramagnetic (PM) phase. Note that in FD and PM phases, the topological spin textures are destabilized by thermal fluctuations, and thus topological charge Q oscillates with a large amplitude. Here, $||Q| - 1| > 0.01$ per skyrmion (or pair of vortices) is used as the judgment criterion for the transformation into FD phase. In addition, the Curie temperatures under different external magnetic fields are estimated to judge the critical temperature of phase transition into PM phase. Importantly, as illustrated in **Figures 3(e,f)**, the Bloch-type topological magnetisms of monolayer MnInP₂Te₆ and MnTIP₂Te₆ realized under different magnetic fields [e.g., LD, SkL, ISk, IBM and VAL phases] can sustain the temperature up to ~70 and 80 K, respectively. With further increasing temperature, topological magnetisms are transformed into FD and PM phases successively. Exceptionally, for monolayer MnInP₂Te₆ under B_z of 1.1-1.3 T, with increasing temperature, the SkL phase is transformed into LD phase first, then FD phase and finally PM phase; see **Figure 3(e)**. In general, these Bloch-type topological magnetisms can exist in a relative wide window of the T-B phase diagrams.

At last, we study the strain effect on the magnetic parameters as well as topological magnetisms of monolayer MnXP₂Te₆. As displayed in **Figures 4(a,b)**, the magnetic parameters of monolayer MnXP₂Te₆ show significant variation as a function of strain. In this regard, the topological spin textures of monolayer MnXP₂Te₆ are expected to vary significantly with strain. **Figure 4(c)** displays

the spin textures of monolayer $\text{MnInP}_2\text{Te}_6$ under different strain and B_z . Under tensile strain, the LD phase remains stable, but no magnetic skyrmion is observed under zero magnetic field. And with the increase of tensile strain, the density of the labyrinth domains increases, and the B_z required for realizing magnetic skyrmions increases gradually. Note that J and B_z are prone to force the parallel arrangement of magnetic moments, while d_{\parallel} induces the magnetic moments in a noncollinear arrangement. As shown in **Figure 4(a)**, increasing tensile strain leads to the increase of d_{\parallel}/J , indicating that DMI plays a more dominated role under tensile strain, which is profit for the emergence of more labyrinth domains.

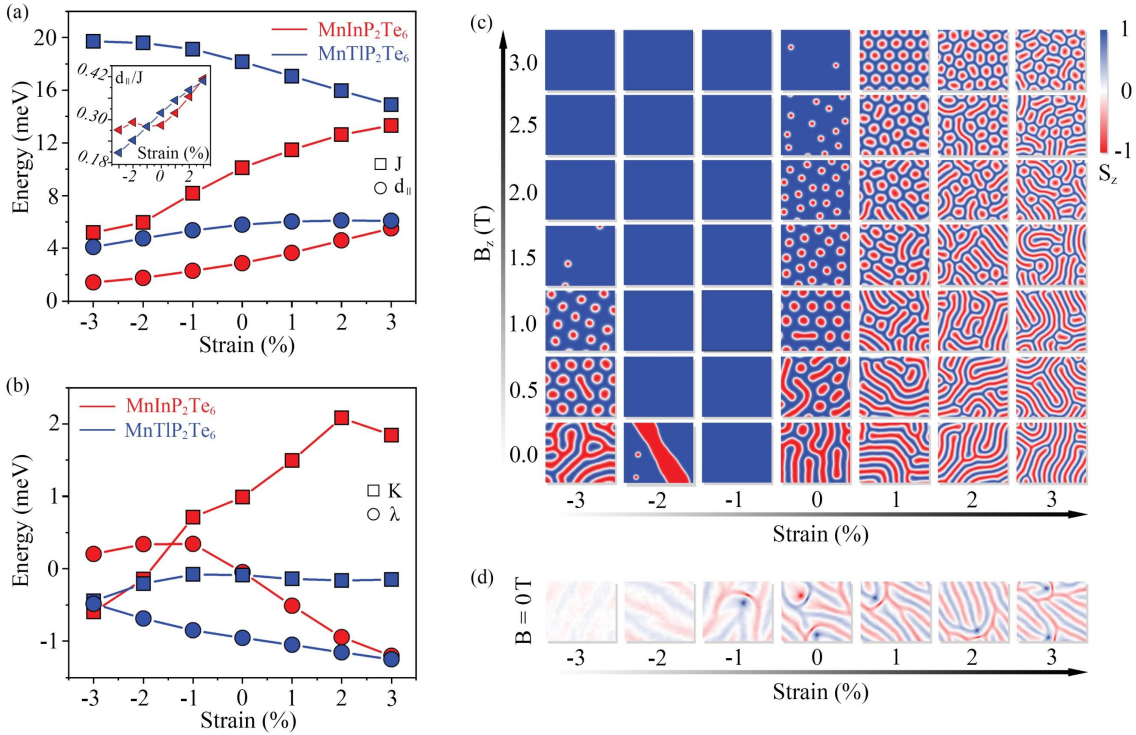


Figure 4 (a) Magnetic parameters J and d_{\parallel} of monolayer MnXP_2Te_6 as a function of strain. Inset in (a) shows d_{\parallel}/J of monolayer MnXP_2Te_6 as a function of strain. (b) Magnetic parameters K and λ of monolayer MnXP_2Te_6 as a function of strain. Spin textures of monolayer (c) $\text{MnInP}_2\text{Te}_6$ and (d) $\text{MnTlP}_2\text{Te}_6$ as a function of strain. Colors in (c,d) indicate the out-of-plane spin components.

For the case under compressive strain, the change of d_{\parallel}/J is relatively slight, and hence the magnetic anisotropy determined by K and λ dominates the evolution of spin patterns with strain. With increasing compressive strain to -1%, λ increases significantly, while K decreases relatively moderate, resulting in a significant increase of out-of-plane magnetic anisotropy; see **Figures 4(b)** and **S8**. As magnetic anisotropy tends to force the magnetic moments to be arranged parallelly, this makes the labyrinth domains and magnetic skyrmions transformed into the FM phase in the absence

of magnetic field [Figure 4(c)]. When further increasing the compressive strain, K and λ decrease simultaneously, resulting in the decrease of out-of-plane magnetic anisotropy. From Figure 4(c), we can see that under -2% strain, the ISk phase containing isolated magnetic skyrmions and a strip domain wall appears at 0 T, and can be transformed into FM phase by applying B_z . It is interesting to point that skyrmion motion can be enhanced by the domain wall, and the accompanying skyrmion Hall effect can thus be suppressed [53]. When further increasing compressive strain to -3%, the LD phase becomes stable again, which results from the continuous decrease of out-of-plane magnetic anisotropy.

For monolayer $\text{MnTIP}_2\text{Te}_6$, with increasing strain, d_{\parallel} increases slightly and K is almost unchanged. Unlike d_{\parallel} and K , J and λ decrease significantly, leading to a monotonic increase of both d_{\parallel} / J and in-plane magnetic anisotropy; see Figures 4(a,b) and S8. Figure 4(d) shows the evaluation of spin textures of monolayer $\text{MnTIP}_2\text{Te}_6$ under various strain. It can be seen that the IBM phase of monolayer $\text{MnTIP}_2\text{Te}_6$ in the absence of magnetic field can be maintained within the strain range of -1% – 3%, while the cases under -3% – -1% strain are transformed into trivial spin patterns. Accordingly, by applying moderate strain, the topological magnetism is controllable in monolayer MnXP_2Te_6 .

Conclusion

To summarize, using first-principles calculations and MC simulations, we report the identification of Bloch-type magnetic skyrmions in two-dimensional lattice of $\text{MnInP}_2\text{Te}_6$. Meanwhile, Bloch-type magnetic bimerons are also observed in monolayer $\text{MnTIP}_2\text{Te}_6$. The underlying physics of such Bloch-type spin configurations are related to the D_3 symmetry. The phase diagrams of these topological magnetisms under magnetic field, temperature and strain are mapped out. Our findings significantly promote the research on topological magnetism in two-dimensional lattice.

Supporting Information

The Supporting Information is available free of charge at []

Competing Interests

The authors declare no competing interests.

Acknowledgement

This work is supported by the National Natural Science Foundation of China (Nos. 12274261 and 12074217), Shandong Provincial Science Foundation for Excellent Young Scholars (No. ZR2020YQ04), Shandong Provincial Natural Science Foundation (Nos. ZR2019QA011), Shandong Provincial Key Research and Development Program (Major Scientific and Technological Innovation Project) (No. 2019JZZY010302), Shandong Provincial QingChuang Technology Support Plan (No. 2021KJ002), and Qilu Young Scholar Program of Shandong University.

References

- [1] Roessler, U. K.; Bogdanov, A.; Pflleiderer, C. Spontaneous skyrmion ground states in magnetic metals. *Nature* **2006**, *442*, 797-801.
- [2] Fert, A.; Reyren, N.; Cros, V. Magnetic skyrmions: advances in physics and potential applications. *Nat. Rev. Mater.* **2017**, *2*, 1.
- [3] Jiang, W.; Chen, G.; Liu, K.; Zang, J.; te Velthuis, S. G. E.; Hoffmann, A. Skyrmions in magnetic multilayers. *Phys. Rep.* **2017**, *704*, 1-49.
- [4] Bogdanov, A. N.; Panagopoulos, C. Physical foundations and basic properties of magnetic skyrmions. *Nat. Rev. Phys.* **2020**, *2*, 492.
- [5] Sampaio, J.; Cros, V.; Rohart, S.; Thiaville, A.; Fert, A. Nucleation, stability and current-induced motion of isolated magnetic skyrmions in nanostructures. *Nat. Nanotechnol.* **2013**, *8*, 839-844.
- [6] Mühlbauer, S.; Binz, B.; Jonietz, F.; Pflleiderer, C.; Rosch, A.; Neubauer, A.; Georgii, R.; Böni, P. Skyrmion lattice in a chiral magnet. *Science* **2009**, *323*, 915-919.
- [7] Nagaosa, N.; Tokura, Y. Topological properties and dynamics of magnetic skyrmions. *Nat. Nanotechnol.* **2013**, *8*, 899-911.
- [8] Zhang, X.; Zhou, Y.; Song, K. M.; Park, T.-E.; Xia, J.; Ezawa, M.; Liu, X.; Zhao, W.; Zhao, G.; Woo, S. Skyrmion-electronics: writing, deleting, reading and processing magnetic skyrmions toward spintronic applications. *J. Phys.: Condens. Matter* **2020**, *32*, 143001.
- [9] Fert, A.; Cros, V.; Sampaio, J. Skyrmions on the track. *Nat. Nanotechnol.* **2013**, *8*, 152.
- [10] Kang, W.; Huang, Y.; Zheng, C.; Lv, W.; Lei, N.; Zhang, Y.; Zhang, X.; Zhou, Y.; Zhao, W. Voltage controlled magnetic skyrmion motion for racetrack memory. *Sci. Rep.* **2016**, *6*, 23164.
- [11] Li, S.; Kang, W.; Zhang, X.; Nie, T.; Zhou, Y.; Wang, K. L.; Zhao, W. Magnetic skyrmions for unconventional computing. *Mater. Horiz.* **2021**, *8*, 854.
- [12] Dong, J.; Zhang, L.; Ding, F. Kinetics of Graphene and 2D Materials Growth. *Adv. Mater.* **2019**, *31*, 1801583.
- [13] Duan, X.; Huang, J.; Xu, B.; Liu, S. A two-dimensional multiferroic metal with voltage-tunable magnetization and metallicity. *Mater. Horiz.* **2021**, *8*, 2316.
- [14] Zhou, J.; Xu, H.; Shi, Y.; Li, J. Terahertz Driven Reversible Topological Phase Transition of Monolayer Transition Metal Dichalcogenides. *Adv. Sci.* **2021**, *8*, 2003832.
- [15] Jiao, Y.; Ma, F.; Bell, J.; Bilic, A.; Du, A. Two-Dimensional Boron Hydride Sheets: High Stability, Massless Dirac Fermions, and Excellent Mechanical Properties. *Angew. Chem.* **2016**, *128*, 10448-10451.
- [16] Ma, F.; Jiao, Y.; Wu, W.; Liu, Y.; Yang, S. A.; Heine, T. Half-Auxeticity and Anisotropic Transport in Pd Decorated Two-Dimensional Boron Sheets. *Nano Lett.* **2021**, *21*, 2356-2362.
- [17] Huang, B.; Clark, G.; Navarro-Moratalla, E.; Klein, D.; Cheng, R.; Seyler, K.; Zhong, D.; Schmidgall, E.; McGuire, M.; Cobden, D.; Yao, W.; Xiao, D.; Jarillo-Herrero, P.; Xu, X. Layer-dependent ferromagnetism in a van der Waals crystal down to the monolayer limit. *Nature* **2017**,

- [18] Ma, Y.; Dai, Y.; Guo, M.; Niu, C.; Zhu, Y.; Huang, B. Evidence of the existence of magnetism in pristine VX_2 monolayers ($X = S, Se$) and their strain-induced tunable magnetic properties. *ACS Nano* **2012**, *6*, 1695-1701.
- [19] Bonilla, M.; Kolekar, S.; Ma, Y.; Diaz, H. C.; Kalappattil, V.; Das, R.; Eggers, T.; Gutierrez, H. R.; Phan, M.-H.; Batzill, M. Strong room-temperature ferromagnetism in VSe_2 monolayers on van der Waals substrates. *Nat. Nanotechnol.* **2018**, *13*, 289-293.
- [20] Deng, Y.; Yu, Y.; Song, Y.; Zhang, J.; Wang, N. Z.; Sun, Z.; Yi, Y.; Wu, Y. Z.; Wu, S.; Zhu, J.; Wang, J.; Chen, X. H.; Zhang, Y. Gate-tunable room-temperature ferromagnetism in two-dimensional Fe_3GeTe_2 . *Nature* **2018**, *563*, 94-99.
- [21] Chen, D.; Wang, J.; Cheng, Z. Controlling bimerons as skyrmion analogues by ferroelectric polarization in 2D van der Waals multiferroic heterostructures. *Nat. Commun.* **2020**, *11*, 5930.
- [22] He, Z.; Dou, K.; Du, W.; Dai, Y.; Huang, B.; Ma, Y. Multiple Topological magnetism in van der Waals heterostructure of $MnTe_2/ZrS_2$. *Nano Lett.* **2023**, *23*, 312-318.
- [23] Li, D.; Haldar, S.; Heinze, S. Strain-driven zero-field near-10 nm Skyrmions in two-dimensional van der Waals heterostructures. *Nano Lett.* **2022**, *22*, 7706-7713.
- [24] Yuan, J.; Yang, Y.; Cai, Y.; Wu, Y.; Chen, Y.; Yan, X.; Shen, L. Intrinsic skyrmions in monolayer Janus magnets. *Phys. Rev. B* **2020**, *101*, 094420.
- [25] Xu, C.; Feng, J.; Prokhorenko, S.; Nahas, Y.; Xiang, H.; Bellaiche, L. Topological spin texture in Janus monolayers of the chromium trihalides $Cr(I, X)_3$. *Phys. Rev. B* **2020**, *101*, 060404(R).
- [26] Du, W.; Dou, K.; He, Z.; Dai, Y.; Huang, B.; Ma, Y. Spontaneous magnetic skyrmions in single-layer $CrInX_3$ ($X = Te, Se$). *Nano Lett.* **2022**, *22*, 3440.
- [27] Sun, W.; Wang, W.; Zang, J.; Li, H.; Zhang, G.; Wang, J.; Cheng, Z. Manipulation of magnetic skyrmion in a 2D van der Waals heterostructure via both electric and magnetic fields. *Adv. Funct. Mater.* **2021**, *31*, 2104452.
- [28] Dou, K.; Du, W.; He, Z.; Dai, Y.; Huang, B.; Ma, Y. Theoretical prediction of antiferromagnetic skyrmion crystal in Janus monolayer $CrSi_2N_2As_2$. *ACS Nano* **2023**, *17*, 1144-1152.
- [29] Liang, J.; Wang, W.; Du, H.; Hallal, A.; Garcia, K.; Chshiev, M.; Fert, A.; Yang, H. Very large Dzyaloshinskii-Moriya interaction in two-dimensional Janus manganese dichalcogenides and its application to realize skyrmion states. *Phys. Rev. B* **2020**, *101*, 184401.
- [30] Liang, J.; Cui, Q.; Yang, H. Electrically switchable Rashba-type Dzyaloshinskii-Moriya interaction and skyrmion in two-dimensional magnetoelectric multiferroics. *Phys. Rev. B* **2020**, *102*, 220409(R).
- [31] Dou, K.; Du, W.; Dai, Y.; Huang, B.; Ma, Y. Two-dimensional magnetoelectric multiferroics in a $MnSTe/In_2Se_3$ heterobilayer with ferroelectrically controllable skyrmions. *Phys. Rev. B* **2022**, *105*, 205427.
- [32] Cui, Q.; Zhu, Y.; Ga, Y.; Liang, J.; Li, P.; Yu, D.; Cui, P.; Yang, H. Anisotropic Dzyaloshinskii-Moriya interaction and topological magnetism in two-dimensional magnets protected by $P\bar{4}m2$ crystal symmetry. *Nano Lett.* **2022**, *22*, 2334-2341.
- [33] Ga, Y.; Cui, Q.; Zhu, Y.; Yu, D.; Wang, L.; Liang, J.; Yang, H. Anisotropic Dzyaloshinskii-Moriya interaction protected by D_{2d} crystal symmetry in two-dimensional ternary compounds. *npj Comput. Mater.* **2022**, *8*, 128.
- [34] Xu, C.; Chen, P.; Tan, H.; Yang, Y.; Xiang, H.; Bellaiche, L. Electric-field switching of magnetic topological charge in type-I multiferroics. *Phys. Rev. Lett.* **2020**, *125*, 037203.
- [35] Amoroso, D.; Barone, P.; Picozzi, S. Spontaneous skyrmionic lattice from anisotropic symmetric exchange in a Ni-halide monolayer. *Nat. Commun.* **2020**, *11*, 5784.

- [36] Tokura, Y.; Kanazawa, N. Magnetic skyrmion materials. *Chem. Rev.* **2021**, *121*, 2857-2897.
- [37] Dzyaloshinsky, I. A thermodynamic theory of “weak” ferromagnetism of antiferromagnetics. *J. Phys. Chem. Solids* **1958**, *4*, 241.
- [38] Moriya, T. Anisotropic superexchange interaction and weak ferromagnetism. *Phys. Rev.* **1960**, *120*, 91.
- [39] Yu, X. Z.; Onose, Y.; Kanazawa, N.; Park, J. H.; Han, J. H.; Matsui, Y.; Nagaosa, N.; Tokura, Y. Real-space observation of a two-dimensional skyrmion crystal. *Nature* **2010**, *465*, 901-904.
- [40] Yu, X. Z.; Onose, Y.; Kimoto, K.; Zhang, W. Z.; Ishiwata, S.; Matsui, Y.; Tokura, Y. Near room-temperature formation of a skyrmion crystal in thin-films of the helimagnet FeGe. *Nat. Mater.* **2011**, *10*, 106-109.
- [41] Seki, S.; Yu, X. Z.; Ishiwata, S.; Tokura, Y. Observation of skyrmions in a multiferroic material. *Science* **2012**, *336*, 198-201.
- [42] Heinze, S.; von Bergmann, K.; Menzel, M.; Brede, J.; Kubetzka, A.; Wiesendanger, R.; Bihlmayer, G.; Blügel, S. Spontaneous atomic-scale magnetic skyrmion lattice in two dimensions. *Nat. Phys.* **2011**, *7*, 713-718.
- [43] Kézsmárki, I.; Bordács, S.; Milde, P.; Neuber, E.; Eng, L. M.; White, J. S.; Rønnow, H. M.; Dewhurst, C. D.; Mochizuki, M.; Yanai, K.; Nakamura, H.; Ehlers, D.; Tsurkan, V.; Loidl, A. Néel-type skyrmion lattice with confined orientation in the polar magnetic semiconductor GaV₄S₈. *Nat. Mater.* **2015**, *14*, 1116-1122.
- [44] Boulle, O.; Vogel, J.; Yang, H. Pizzini, S.; de Souza Chaves, D.; Locatelli, A.; Menteş, T.; Sala, A.; Buda-Prejbeanu, L.; Klein, O.; Belmeguenai, M.; Roussigné, Y.; Stashkevich, A.; Chérif, S.; Aballe, L.; Foerster, M.; Chshiev, M.; Auffret, S.; Miron, I.; Gaudin, G. Room-temperature chiral magnetic skyrmions in ultrathin magnetic nanostructures. *Nat. Nanotechnol.* **2016**, *11*, 449-454.
- [45] Wang, L.; et al. Ferroelectrically tunable magnetic skyrmions in ultrathin oxide heterostructures. *Nat. Mater.* **2018**, *17*, 1087-1094.
- [46] Ohara, K.; Zhang, X.; Chen, Y.; Kato, S.; Xia, J.; Ezawa, M.; Tretiakov, O. A.; Hou, Z.; Zhou, Y.; Zhao, G.; Yang, J.; Liu, X. Reversible transformation between isolated skyrmions and bimerons. *Nano Lett.* **2022**, *22*, 8559-8566.
- [47] Nayak, A. K.; Kumar, V.; Ma, T.; Werner, P.; Pippel, E.; Sahoo, R.; Damay, F.; Rößler, U. K.; Felser, C.; Parkin, S. S. P. Magnetic antiskyrmions above room temperature in tetragonal heusler materials. *Nature* **2017**, *548*, 561-566.
- [48] Peng, L.; Takagi, R.; Koshibae, W.; Shibata, K.; Nakajima, K.; Arima, T.-h.; Nagaosa, N.; Seki, S.; Yu, X.; Tokura, Y. Controlled transformation of skyrmions and antiskyrmions in a non-centrosymmetric magnet. *Nat. Nanotechnol.* **2020**, *15*, 181-186.
- [49] Zhou, W.; Zheng, G.; Li, A.; Zhang, D.; Ouyang, F. Orbital contribution to the regulation of the spin-valley coupling in antiferromagnetic monolayer MnPTe₃. *Phys. Rev. B* **2023**, *107*, 035139.
- [50] Fert, A.; Levy, P. M. Role of anisotropic exchange interactions in determining the properties of spin-glasses. *Phys. Rev. Lett.* **1980**, *44*, 1538.
- [51] Levy, P. M.; Fert, A. Anisotropy induced by nonmagnetic impurities in CuMn spin-glass alloys. *Phys. Rev. B* **1981**, *23*, 4667.
- [52] Berg B.; Lüscher, M. Definition and statistical distributions of a topological number in the lattice O(3) σ -model. *Nuclear Phys. B* **1981**, *190*, 412-424.
- [53] Xing, X.; Akerman, J.; Zhou, Y. Enhanced skyrmion motion via strip domain wall. *Phys. Rev. B* **2020**, *101*, 214432.